



Optimization of the Injectors Position for an Electric Arc Furnace by using CFD Simulation

G. Coskun, C. Sarikaya, E. Buyukkaya[†] and H. Kucuk

Department of Mechanical Engineering, Sakarya University, Sakarya, 54050, Turkey

[†]Corresponding Author Email: ebkaya@sakarya.edu.tr

(Received June 15, 2022; accepted September 25, 2022)

ABSTRACT

In this study, complex processes in a typical Electric Arc Furnace (EAF) such as combustion, radiation, heat, and mass transfer were solved and the optimum injector location was found using computational fluid dynamics (CFD). The main aim of the injection optimization was to improve the thermal performance and the metallurgical process by changing the injection angle, the central angle of the injector (CAI), and injector length. Fifteen parametric cases were predicted and analyzed for optimization study. To decrease each simulation solution time of each cases, a polyhedral mesh structure was used instead of tetrahedral mesh for the EAF geometry. Thus, the total element number of the model was decreased by 1/5 while providing faster and unchanging results compared to the case with a tetrahedral mesh structure. The response surface optimization method was used for the optimization study. As a result, the optimum injector positioning was obtained as injection angle: -45° , injector length 614 mm, and CAI: 60° .

Keywords: Electric Arc Furnace (EAF); Computational Fluid Dynamics (CFD); Fine coal combustion; Injectors; Optimization.

NOMENCLATURE

a	absorption coefficient	R_i	net rate of production of species i
A_r	pre-exponential factor	S_h	the heat of chemical reaction
C	linear-anisotropic phase function coefficient	S_i	Source term
$C_{1\epsilon}$	constant	S_k	Source term
C_2	constant	S_m	source term
$C_{3\epsilon}$	constant	S_ϵ	Source term
E_r	activation energy	$v''_{i,r}$	product species stoichiometric coefficient
F	external body forces	$v'_{R,r}$	stoichiometric coefficient for reactant i
G	incident radiation	Y_p	mass fraction of any product species
G_b	production of turb. kin. en. due to buoyancy	Y_R	mass fraction of particular reactant
G_k	production of turbulent kinetic energy	$\bar{\tau}$	stress tensor
I	unit tensor	ϵ	turbulent dissipation rate
\vec{J}_j	diffusion flux of species j	σ_k	constant
k	turbulent kinetic energy	σ_s	scattering coefficient
k_{eff}	effective conductivity	σ_ϵ	constant
$M_{w,i}$	molecular weight of species i	ρ	density
N	number of reactions	μ	molecular viscosity
p	static pressure	μ_t	eddy viscosity
R	universal gas constant	β_r	temperature exponent

1. INTRODUCTION

Both a large amount of chemical energy and electrical energy are needed to heat the scrap to the melting temperature at the industrial electric arc furnace (EAF). About 30% of the world's steel manufacturing is provided by EAF facilities (Hites 2020). Approximately three-quarters of the total steel requirements are supplied in these facilities, and the rest is produced in the iron-steel production industry. A modern high capacity furnace can process 350 tons of scrap per loading. This process takes approximately 50-60 minutes and the consumed energy to produce per ton of steel is 6-8 GJ (Fruehan 1998) This is just half of the consumption at iron-steel production factory, and also the equivalent to electrical demand of a city with a hundred thousand residents. The total crude steel production around the world is approximately 1.85 billion tons/year. This is considered as a high energy consumption that cannot be underestimated (Worldsteel association 2019)

The statistics of the iron-steel sector show that steel production is increasing each year. There is also a considerable magnitude of energy consumption. In this case, reducing the amount of energy consumption per steel production is an important job. Besides, approximately 50% of the available energy is wasted for various reasons during the EAF steel production (Çamdali and Tunç 2001). In the EAF steel-making, less electricity usage and more efficient combustion strategies are important in terms of energy-saving. There are some methods for reducing the melting period thus the cost of the melting process for per ton scrap can be decreased. In the EAF, total energy input consists of electrical energy and chemical energy is about 60-65% and 30-35%, respectively (Zhang *et al.* 2013). Also, to increase the efficiency of EAF, the energy gain by the chemical reactions should be increased while not changing the electrical energy consumption. For this purpose, avoiding a high energy loss during the flat bath phase, determining the optimum location and injection angle of injectors must be taken into consideration.

With the development of computer and software technologies at the beginning of the new century, the CFD method has been used to make arc furnaces more efficient. Alexis *et al.* (2000) used mass, momentum, and energy conservation equations with the Maxwell equation to calculate plasma temperature, pressure, and the velocity of the scrap during the EAF process. They used a simple axisymmetric two-dimensional geometry. In their model, the arc was treated as a fluid with temperature-dependent thermodynamic properties. They predicted heat transfer for different currents and the arc lengths and found that arc efficiency is higher for lower power input. Li and Fruehan (2003) used a three-dimensional model of a cylindrical EAF that contained three electrodes but the liquid metal reservoir was not included. Through this model, a detailed analysis of the CFD has led to the simultaneous solution of the post-combustion reactions, flow, radiation, and convective heat transfer in the EAFs gas volume. The results of the

analysis showed that most of the available energy leaves the EAF from the exhaust elbow by flue gas and from the side walls and roof by radiation. It has been reported that 30% of the total energy is released from the furnace by flue gases, 56% from the side and roof walls, only 12% is transferred to the melt the surface by radiation and chemical energy. It is concluded that the thermal radiation by the electrodes is important to melt scrap pile. Guo and Irons (2003) used a 3D CFD model to define radiation energy distribution in a typical industrial EAF. They modeled the EAF geometry which has three graphite electrodes and slag volume. They investigated the radiation energy distribution of water-cooled side walls and furnace roof. They determined that the maximum temperature of graphite electrodes is approximately 3600 K. Furthermore, they calculated the conduction heat loss from electrodes as around 3.0% of total electrical energy. Wang *et al.* (2014) used a CFD simulation of 1500 - 3000 kVA EAF to investigate MgO production. They predicted the temperature distribution of EAFs by calculating electromagnetic fields by the finite element method. They found that the high power EAF and larger size molten bath have positive effects on melt, energy conservation, and output. However, their simulation strategy doesn't involve the combustion process which can also affect the MgO production. Transient CFD simulation prepared by Carmona and Cortés (2014) to investigate the secondary aluminum melting process by a plasma torch. By using both complex and simplified models they tested the effects of simplifying methods on the consistency with experimental results. They obtained the most accurate results from the most complex models. However, the complexity caused 3.6 times more computational cost than the effective coefficients model. Odenthal *et al.* (2017) simulated a supersonic oxygen jet injection by using the CFD with a Large Eddy Simulation (LES) turbulence model. They adapted the LES turbulence CFD simulation results of time-averaged values for the jet momentum into a holistic Reynolds-Averaged Navier-Stokes (RANS) model of an EAF as input parameter and calculated the entire furnace with the continuous phases of melt, slag, and oxygen. They reported that the results of their CFD models couldn't be combined due to scale-transition phenomena and the lack of computational capacity; however, important results for EAFs can be obtained from their study. Wei *et al.* (2018) simulated coherent jets flow and combustion in EAF by using a one-step and detailed chemical mechanism with a 2D CFD model. In their study, CFD results for velocity and temperature distribution of the coherent jet at the jet centerline were compared with experimental results. They obtained a better agreement with detailed chemical reactions than one-step combustion.

Pretorius and Carlisle (1998) stated that injectors have critical importance for creating the insulation layer by forming a foamy slag, increasing the melting capacity, and removing cold regions of the melt. Because foamy slag decreases the radiation losses by isolating the light beams. Also, it allows higher power input and efficient energy transfer by

increasing the heat transfer between electrodes and the molten metal. Injected fine coal provides extra energy input with chemical reactions. CO occurs in the melt volume by oxidation reactions and helps to form a foamy slag layer. The works of Kipepe and Pan (2014), Rahman (2010) and Sanche *et al.* (2012) indicated that a foamy slag layer protects refractors from arc combustion by covering electric arc, increases liquid steel quality by absorbing deoxidation products (SiO₂, Al₂O₃) and inclusions, makes dephosphorization in furnace and desulphurization in the melting pot, protects the metal from oxidation, nitrogen, and hydrogen absorption and decreases the thermal losses through isolating the melt. Zhang *et al.* (2013) stated that chemical reactions and the foamy slag can provide electrical energy saving by about 4-5% throughout the carbon injection in EAF. The energy-saving is possible by more chemical energy utilization as an extra energy input when the arc immerses into the slag. Generally, the injection of fine coal and oxygen into melt from a certain height and angle is between -30° and -45° to provide a foamy slag. Determining the optimum positions of injectors is important to provide a thick and high-quality foamy slag layer.

The literature review revealed that the simulation studies on EAF were focused on specific physical phenomena like electric arc or combustion and post-combustion modeling because of the complexity of the system. In an earlier study (Yigit *et al.* 2015), energy input from electric arc and combustion processes of the flat-bath phase, during which high energy input and steel quality started to form, was simulated simultaneously. In this way, it is possible to investigate the optimum injector position which increases combustion efficiency as well as the coal and O₂ input to the melt by using CFD simulations. In this study, the injector position parameters as injection angles, the central angle of the injector (CAI), and injector length were optimized to increase the melt temperature and the amount of fine coal input to the melt. As a result of the optimization study, the average surface temperature of the melt, correlated with the melt temperature, was increased and the number of cold regions was decreased. Furthermore, the amount of the fine coal input to the melt which could help to form more foam was increased.

2. NUMERICAL MODEL

The numerical model of the EAF needs to include many equations to solve combustion reactions, radiation heat transfer, and turbulent flows. Solving the EAF model using all these equations simultaneously is almost impossible due to the slow convergence. To resolve the convergence errors, equations were progressively activated. First, the flow analysis was solved for sufficient iterations, then the energy equation. And finally, the radiation equations were activated. The COUPLED algorithm was used for pressure velocity coupling. CFD simulations were simplified by using some assumptions as a steady-state condition, non-compressible flow, six-step combustion reaction

model, RANS turbulence model, P1 radiation model, and a single-phase flow model.

2.1 Governing Equations

In the CFD analysis of the EAF, it is necessary to select accurate models of the turbulence flow, combustion reactions, radiation heat transfer, and other physical phenomena. In this study, equations for mass, momentum, and energy conservation were solved by following governing equations. The mass conservation equation is expressed as follows:

$$\frac{\partial \rho}{\partial t} + \nabla \cdot (\rho \vec{v}) = S_m \quad (1)$$

where ρ is the density of the fluid and S_m is the source term.

The momentum conservation equation is expressed as follows:

$$\frac{\partial}{\partial t}(\rho \vec{v}) + \nabla \cdot (\rho \vec{v} \vec{v}) = -\nabla p + \nabla \cdot (\bar{\tau}) + \rho \vec{g} + \vec{F} \quad (2)$$

Here p represents static pressure, $\bar{\tau}$ is the stress tensor, $\rho \vec{g}$ and \vec{F} are the gravitational body force and external body forces, respectively.

The stress tensor, $\bar{\tau}$ is expressed as follows:

$$\bar{\tau} = \mu \left[(\nabla \vec{v} + \nabla \vec{v}^T) - \frac{2}{3} \nabla \cdot \vec{v} I \right] \quad (3)$$

where μ is the molecular viscosity and, I is the unit tensor.

The energy equation is expressed as follows:

$$\frac{\partial}{\partial t}(\rho E) + \nabla \cdot (\vec{v}(\rho E + p)) = \nabla \cdot \left(k_{eff} \nabla T - \sum_j h_j \vec{j}_j + (\bar{\tau}_{eff} \cdot \vec{v}) \right) + S_h \quad (4)$$

where k_{eff} represents effective conductivity and \vec{j}_j is the diffusion flux of species j . S_h represents the heat of chemical reactions and any other volumetric heat sources.

Alam *et al.* (2010) and Zhang *et al.* (2013) used RANS $k-\varepsilon$ turbulence models for combustion with coal injection CFD simulations. Askarova *et al.* (2016) used the $k-\varepsilon$ turbulence model to simulate the turbulent flow of pulverized coal combustion in the combustion chamber of a Power Plant. Yangaz *et al.* (2019) used the $k-\varepsilon$ turbulence model to obtain temperature distribution in an industrial burner CFD model. Therefore, the realizable $k-\varepsilon$ has been used to solve turbulence which was proposed by Shih *et al.* (1995) and Kim *et al.* (1997). The turbulence kinetic energy (k) and its dissipation rate (ε) are obtained by the following equations:

$$\frac{\partial(\rho k)}{\partial t} + \frac{\partial(\rho k v_i)}{\partial x_i} = \frac{\partial}{\partial x_j} \left[\left(\mu + \frac{\mu_t}{\sigma_k} \right) \frac{\partial k}{\partial x_i} \right] + G_k + G_b - \rho \varepsilon - Y_M + S_k$$

$$\frac{\partial(\rho\varepsilon)}{\partial t} + \frac{\partial(\rho\varepsilon u)}{\partial x_j} = \frac{\partial}{\partial x_j} \left[\left(\mu + \frac{\mu_t}{\sigma_\varepsilon} \right) \frac{\partial \varepsilon}{\partial x_j} \right] + \rho C_{1\varepsilon} S_\varepsilon - \rho C_{2\varepsilon} \frac{\varepsilon^2}{k + \sqrt{v\varepsilon}} + C_{1\varepsilon} \frac{\varepsilon}{k} C_{3\varepsilon} G_b + S_\varepsilon \quad (5)$$

Where, G_k represents the generation of turbulence kinetic energy, G_b represents the generation of turbulence kinetic energy via buoyancy and Y_M represents the contribution of the fluctuating dilatation. $C_{1\varepsilon}$, $C_{2\varepsilon}$, and $C_{3\varepsilon}$ are constants. Also σ_k and σ_ε are the turbulent Prandtl numbers for k and ε respectively. S_k and S_ε are user-defined source terms have a value of 0.7. After determining k and ε , the following equation calculates eddy viscosity (μ_t):

$$\mu_t = \rho C_\mu \frac{\varepsilon^2}{k} \quad (6)$$

Here C_μ is a constant.

The model constants $C_{1\varepsilon}$, $C_{2\varepsilon}$, C_μ , σ_k and σ_ε have the default values respectively 1.44, 1.92, 0.09, 1 and 1.3 recommended by [Lauder and Spalding \(1972\)](#).

2.2 Radiation Modeling

The radiative heat transfer is important when the inside of furnace temperature reaches high temperature (~2000 K) due to the electrodes and chemical reactions. [Scheepers *et al.* \(2010\)](#) indicated that multiple simulation to use the P1 model that accurately solves the radiation heat transfer in the EAF. In their study, multiple simulations showed that the P1 model (with default settings provided by Ansys Fluent) solved the radiation effectively. [Falihatkar and Ahmadikia \(2014\)](#) used the P1 radiation model to solve the radiative properties of the mixture resulting from combustion in a burner. Because of the low computational cost and previously used in EAF CFD simulations in the literature, the P1 model was chosen for the radiation calculations generated from the electrodes and chemical reactions in the solution domain in the current study. The radiation heat flux is expressed as follows:

$$q_r = -\frac{1}{3(a + \sigma_s) - C\sigma_s} \nabla G \quad (7)$$

Here a is the absorption coefficient, σ_s is the scattering coefficient, G is the incident radiation. The linear-anisotropic phase function coefficient C is ranges from -1 to 1. A positive value means that more radiant energy is scattered backwards, and a negative value vice versa. A value of zero defines isotropic scattering, which is the default in the software ([Ansys Fluent Theory Guide, 2009](#)).

In the current simulations the internal emissivity radiation was applied at each wall. At the slag surface, the lower and the upper bath walls emissivity was used as 0.7, while the granite electrode walls were 0.85 ([Guo and Irons 2003](#)).

2.3 Combustion Modeling

The species transport model was used for coal combustion. The local mass fractions Y_i for each

species can be calculated by the following conservation equation:

$$\frac{\partial}{\partial t} (\rho Y_i) + \nabla \cdot (\rho \vec{v} Y_i) = -\nabla \cdot \vec{J}_i + R_i + S_i \quad (8)$$

Here the net rate of production of species i by the chemical reaction representing by R_i and the rate of creation with the addition from the dispersed phase representing by S_i .

Finite-Rate/Eddy-Dissipation model was used to calculate reaction rates considering the rate-controlling mechanism, that may be either the chemical kinetics or the turbulent mixing by solving both the Arrhenius kinetic and eddy-dissipation. The Arrhenius kinetic and eddy-dissipation rates are expressed as follows:

$$k_{f,r} = A_r T^{\beta_r} e^{-E_r/RT} \quad (9)$$

$$R_{i,r} = 4v'_{i,r} M_{w,i} \rho \frac{\varepsilon}{k} \min \left[\frac{Y_R}{v'_{R,r} M_{w,R}}, \frac{\sum_P Y_P}{2 \sum_j^N v''_{j,r} M_{w,R}} \right] \quad (10)$$

Where A_r is the pre-exponential factor, β_r is temperature exponent, E_r is the activation energy for the reaction, R is the universal gas constant, Y_P is the mass fraction of any product species, Y_R is the mass fraction of a particular reactant, N is the number of reaction, $v'_{i,r}$ is the stoichiometric coefficient for reactant i , $v''_{j,r}$ is the product species stoichiometric coefficient, $M_{w,i}$ is the molecular weight of species i .

Global kinetics for surface reactions of injected coal and oxygen (O₂) in the furnace, represented as Arrhenius expressions, were based on the pre-exponential factors and activation energies are listed in Table 1. The chemical reactions enabled the formation of six reactions; three of them are heterogeneous particle reactions ([Zhang *et al.* 2013](#)) and three of them are gas-phase reactions. Due to the quantities of the fixed carbon and volatile matter (m_{v,vol}) the coal was simply classified as a single species in the current simulations. m_{v,vol} break up was assumed to be a single hypothetical hydrocarbon component consisting of Carbon (C), Hydrogen (H), and O₂. The Coal particles that were injected into the computational volume, volatile matters initially convert to a pseudo gas-phase species using the constant rate devolatilization model. Detailed information on coal chemistry of Ansys Fluent can be found in the study of [Lee *et al.* \(2010\)](#). Reaction rates for gas-phase and particle surface reactions were obtained from [Ansys Fluent user manual \(2013\)](#) and [Lee *et al.* \(2010\)](#).

2.4 Computational Domain

The exact measurement of the EAF geometry was supplied from CVS Technologies, and the geometry of the model was generated using the software ANSYS Designmodeler. The solution domain of the furnace shown in Fig. 1 was modeled with an inner height of 3505.25 mm, an inner radius of 3600 mm, and a melt surface radius of 3080 mm. The geometry

Table 1 Gas-phase and particle surface reactions

Gas-Phase Reactions				
Reaction Number		A	Ea(kj/mol)	
1	$m_{v,v_{vol}} + 1.706O_2 \rightarrow CO_2 + 1.543H_2O$	2.119e+11	202.7	
2	$H_2 + 0.5O_2 \rightarrow H_2O$	1e+15	1	
3	$CO + 0.5O_2 \rightarrow CO_2$	1.30E+11	1.26	
Heterogeneous particle surface reactions				
Reaction Number		A	Ea(kj/mol)	Diffusion rate constant ($m^3/K^{0.75} s$)
4	$C(s) + 0.5O_2 \rightarrow CO$	0.052	1.33	5e-12
5	$C(s) + CO_2 \rightarrow 2CO$	4.4	1.62	5e-12
6	$C(s) + H_2O \rightarrow H_2 + CO$	1.33	1.47	5e-12

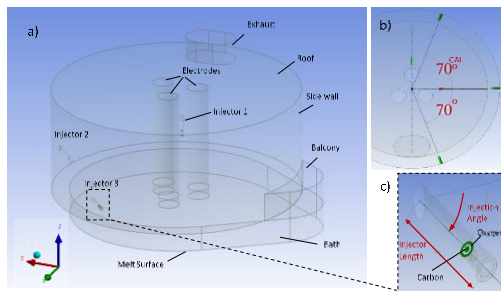


Fig. 1. a) Solution domain of the EAF b) Centre angle of the injector (CAI) c) Injection angle (IA) and injector length (IL).

of the graphite electrodes within the solution domain is a cylinder with an arc column height of 320 mm and an electrode radius of 305 mm.

In the model, three injectors blowing oxygen and fine coal into the furnace were located on the furnace wall, as shown in Fig. 1. The angle between the injectors is called the center angle of the injector (CAI) and injectors 1, 2, and 3 have angles of 70° , 0° , -70° , respectively. All injectors were set above the melt's surface to have a height of 1.07 m, injector length of 614 mm, and injection angle of -45° with respect to the XY-plane. One of the purposes of this study is to obtain the temperature distribution of the surface above the melt. Therefore, the surface that owns the melt properties was set instead of the melt volume and the slag volume in the solution domain. Three electrodes generate electric arc from their bottom surfaces and heat flux was defined as electrical power and it was set constant.

2.5 Boundary Conditions

In the model, the flow rates of injected coal and oxygen were supplied from CVS Technologies. The discrete phase model (DPM) which is a useful method to simulate the carbon particle trajectory used for the simulations. The minimum, the maximum, and the mean particle diameters were chosen as $70e-06$ m, $200e-06$, and $134e-06$ m, respectively. Each injector blows 30 kg/min of fine coal into the furnace. The velocity of oxygen via the injectors has only an axial component and was set to the value of 137 m/s so that radial velocities were defined to be zero. Hydraulic diameter and turbulence intensity were selected for the

specification of turbulence at the inlet boundary. The temperatures of the bath, balcony, side wall, and roof were set constant and had values of 873 K, 773 K, and 393K, respectively. Besides, the convective heat transfer at the melt surface properties was set as convective heat transfer coefficient of $50 W/m^2K$, free stream temperature of 323 K for the accurate analysis of the heat passing through the melt. Also, the conduction through the EAF shell was enabled at the melt surface with the thermal conductivity of $50 W/mK$, thickness of 1.5 m. In the EAF, electrodes have a total electrical energy of 100 MW equaling to a uniform heat flux of $1.15e+8 W/m^2$ at the bottom surface of each electrode.

In the EAF, carbon monoxide enters into the furnace from the melt surface that is generated due to the oxidation of iron ($FeO + C \rightarrow Fe + CO$) in the melt. In the steel-making process, the amount of incoming carbon monoxide from the melt is about 1.5 kmol for per ton of scrap. For this reason, carbon monoxide mass flux of $0.021455 kg/m^2\cdot s$ entering into the solution domain was defined on the melt surface.

2.6 Mesh Structure of the CFD Model

In terms of the accuracy of CFD solutions, the quality of the mesh is known to be important. In some regions in the solution domain a finer mesh is needed for a precise calculation of the chemical reactions, thus smaller elements were created at the top region of the melt surface, around the arc, and the exit of the injectors, as shown in Fig. 2. In the first step of the ANSYS Mesh Software, the structural mesh for the bath and the exhaust, also tetrahedral mesh for the rest of the solution domain were set. The mesh structure of the EAF model in the current study was optimized to decrease the simulation time. For this purpose, the tetrahedral mesh structure was transferred into a polyhedral mesh structure. Firstly, CFD results obtained from both models with the same meshing operation but different structures, which are tetrahedral and polyhedral, were compared. CFD solutions show that polyhedral and tetrahedral mesh structured models had similar results. The number of elements was decreased by 1/5 while converting the mesh structure tetrahedral to polyhedral. In connection with the increasing total number of elements, total solution time and RAM usage were significantly decreased. Fig. 2 shows two

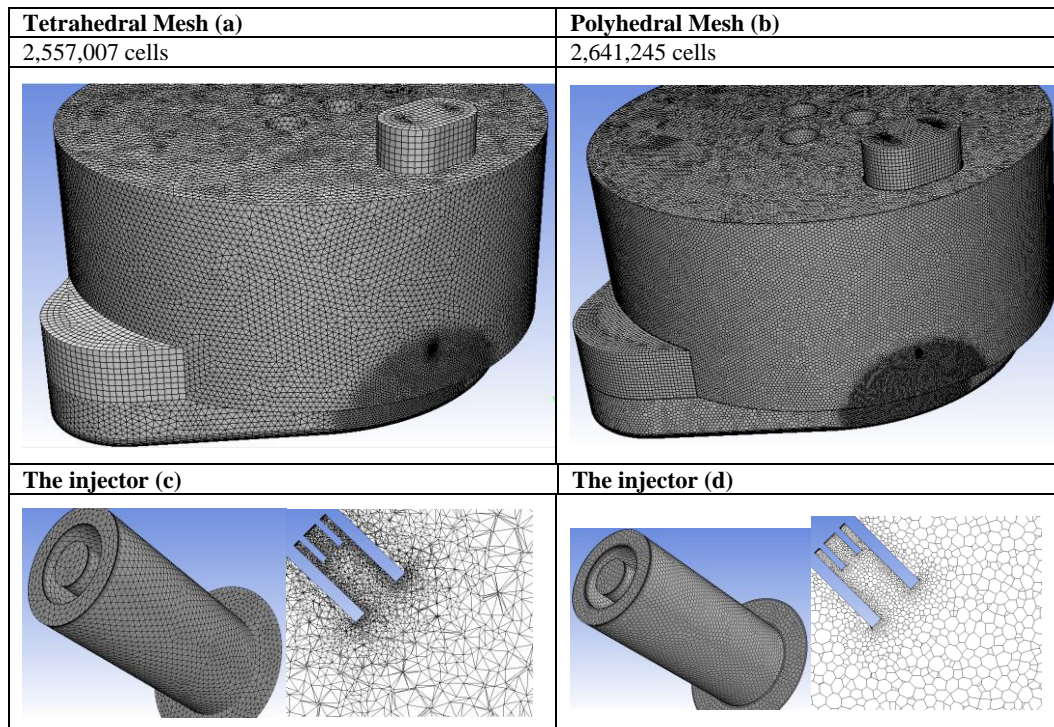


Fig. 2. Discretized geometry with (a) tetrahedral and (b) polyhedral cells of the model.

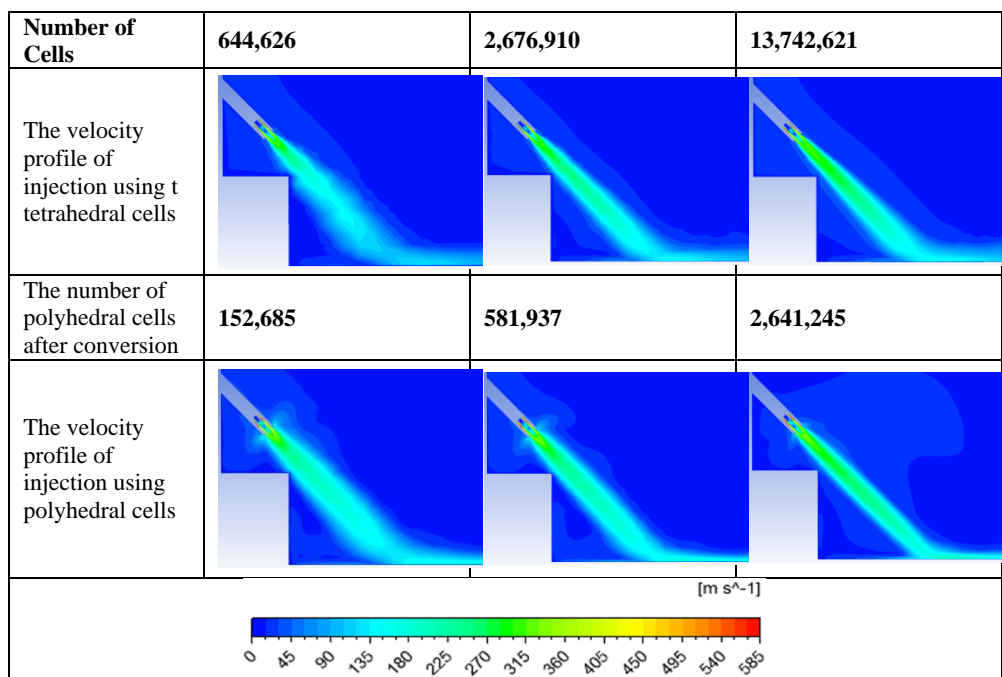


Fig. 3. Effects of the cell geometry and number on the velocity profile of injection.

types of discretized models that have tetrahedral and polyhedral meshes of an almost equal number of cells. Besides, in Fig. 2b, the mesh consisting of 2.5 million polyhedral cells are converted from 13.7 million tetrahedral cells.

Before starting the analysis, the mesh independency on the simulation results was examined by changing the number of cells. Fig. 3 shows the velocity profile of the injected flow for a different number of tetrahedral and polyhedral cells. The more reliable

velocity profile of the flow is obtained by increasing the number of cells for both tetrahedral and polyhedral meshes. It is seen that the velocity profiles of the models consisting of 13.7 million tetrahedral cells and 2.6 million polyhedral cells have an accurate flow of the injection. Besides, it is understood that the velocity profile obtained with the number of 2.6 million polyhedral cells is quite similar to the velocity profile obtained in the study of [Campolo *et al.* \(2007\)](#) They used structural mesh

Table 2. The Effects of cell geometry and number on the simulation results

Model Number	Tetrahedral Cell Number	Polyhedral Cell Number	Fine Coal Input to the Melt [kg/s]	Mass Fraction of CO ₂ in Exhaust	Average Surface Temperature of the Melt [K]	Mass Fraction of O ₂ in the furnace	Mass Fraction of CO ₂ in the furnace
1	1,246,456	278,767	0.6563	0.1184	1875.1	0.8060	0.1861
2	1,549,776	341,767	0.6714	0.1503	1871.8	0.7853	0.2007
3	2,676,910	581,937	0.5622	0.1395	1871.1	0.7865	0.2002
4	4,968,047	1,013,876	0.8567	0.1322	1870.6	0.7797	0.2111
5	13,742,621	2,641,245	0.8164	0.1305	1870.3	0.7704	0.2145
6	30,351,121	5,580,840	0.8273	0.1295	1870.2	0.7695	0.2132

strategy at a partial volume of the furnace geometry including injector volume.

As mentioned above, the mesh independency on the simulation results was tested by using various cell numbers in the solution domain. For this purpose, the results of six models that have different cell numbers were obtained are given in Table 2. The differences between the model consisting of 2.6 polyhedral cells and the model that has higher cell numbers can be ignored according to results. As a result, the mesh independent model (Model 5) was selected for the optimization analysis of the injectors.

3. OPTIMIZATION STUDY AND RESULTS

The main aim of this study is to optimize the injector position for the typical EAF with changing injection angle, CAI, and injector length to increase the temperature distribution on the melt surface and amount of the fine coal input to the melt. Increasing coal input to the melt has a positive effect on forming more foam on the melt surface and increasing carbon amount in the melt. These are decreasing total process time. The optimum injector position which helps to increase the melt surface temperature can provide to reach desired melt temperature with lower electrical energy at electrodes. At the same time, an increase of the coal input to melt could decrease the time of the process to obtain the desired metallurgical characteristics of the melt and provides less O₂ usage.

The actual injector location of the EAF was injection angle: -45°, injector length 514 mm, and CAI: 70°. Many numerical models having lower and upper bounds of these three parameters at a wide range were solved before the optimization study and parameter ranges were dropped according to results. Thus, the lower and upper bounds of three parameters for optimization studies were defined as -45° and -35° of angles between injectors and molten surface (injection angle), 60° and 80° of CAI 414 mm and 614 mm of injector length, respectively.

In the ANSYS-Workbench optimization tool, fifteen different design points were created via the Response Surface Optimization method with the face-centered standard mode under the central composite design. Genetic Aggregation algorithm is used to obtain sub-data in response surface optimization method. The CFD simulations of these cases identified with

different design points were made individually and the results are presented in Table 3. While the injector length increases, the coal input to melt also increased. This is because of the fact that the traveled distance and thus the reaction time of O₂ and fine coal in the gas volume were shortened. It was also observed that the surface temperature of melt was not affected by changing the injector length. Even around of injection region, it was found that there was a slight increase in the average surface temperature of the melt. It is noteworthy that the injection angle is an affecting parameter for the coal input to the melt. As the injection angle decreases to -45°, it was seen that there was an increase in the amount of the coal mass input to melt. It was understood that the decrease at the injection angle generally increases the average surface temperature of the melt. This effect is especially evident in cases with an injector length of 614 mm. As a result, while the injector length increases and the injector angle decreases, the average surface temperature increased as expected.

Besides, for different injector positions, it was understood that the heat of reactions via the combustion of fine coal and O₂ changes were around approximately ± 1MW. This amount corresponds approximately to 0.85% of the total energy input in the EAF. In addition, it was inferred that an increase in the amount of mass input creates an insignificant cooling effect for the melt. Because the area that injected and unburned mass of O₂ and coal reached on the melt surface cool down the average surface temperature. Consequently, the increase of the coal input to the melt is a more valuable parameter that should be focused on in terms of metallurgical processes in EAF instead of the increase of average surface temperature on the melt by just 2%.

Using the results of 15 different simulations, 3000 sub-data created via the screening method in ANSYS optimization software were evaluated according to the determined multi-objective, which is the maximum average surface temperature of the melt and the maximum mass flow of the coal input to melt. Table 4 presents the three best solutions for multi-objective. The best results for both evaluation criteria were obtained with the injector length of 614 mm, CAI of 60°, and injection angle of - 45°. The average surface temperature of melt increased from 1870 K to 1901 K while the injector was 100 mm longer than its original length of 514 mm and the CAI

Table 3. Results of simulations for 15 design points

Design Points	Inputs			Outputs			
	Injection Length [mm]	Injector Angle [°]	CAI [°]	The average surface temperature of melt [K]	Fine coal mass input to melt [kg/s]	Fine coal burned mass [kg/s]	The heat of reaction [kW]
1	414	-45	60	1891.4	0.192	1.307	15.180
2	414	-45	80	1895.1	0.296	1.203	18.213
3	414	-40	70	1882.1	0.288	1.211	16.864
4	414	-35	60	1874.2	0.137	1.362	16.956
5	414	-35	80	1889.0	0.105	1.394	16.598
6	514	-45	70	1870.3	0.176	1.323	18.527
7	514	-40	60	1910.7	0.167	1.332	18.35
8	514	-40	70	1860.3	0.090	1.409	22.593
9	514	-40	80	1904.0	0.168	1.331	17.279
10	514	-35	70	1862.7	0.189	1.310	17.985
11	614	-45	60	1901.0	0.377	1.122	16.415
12	614	-45	80	1904.8	0.333	1.166	16.038
13	614	-40	70	1888.1	0.248	1.251	16.854
14	614	-35	60	1866.0	0.254	1.245	15.232
15	614	-35	80	1878.1	0.165	1.334	16.838

Table 4 Optimum data points obtained based on multi-objective optimization

	Best Solution 1		Best Solution 2		Best Solution 3	
Injector Length [mm]	614		606.57		572.43	
Injection Angle [°]	-45		-44.263		-44	
CAI [°]	60		79.732		60.418	
Average surface temperature of melt [K]	★ ★	1901.0	★ ★	1904.3	★	1896.1
Fine coal mass input [kg/s]	★ ★ ★	0.377188	★ ★	0.32023	★ ★	0.32129

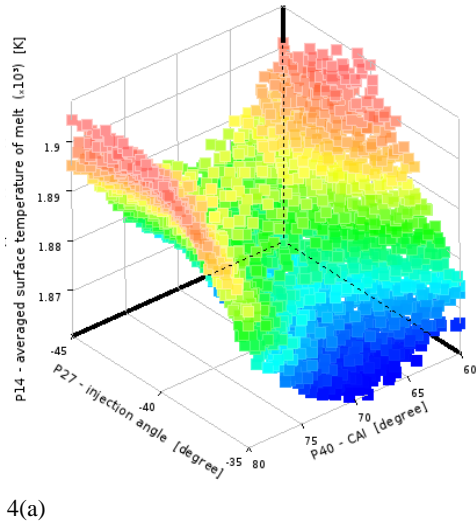
angle was reduced from 70° to 60°. These changes on the injector location also increased the amount of coal input to the melt is about 2.14 times that increased from 0.176 kg/s to 0.377 kg/s.

Based on the above optimization results, the changes on the average surface temperature of the melt and the coal mass input to melt surface under two injector position angles, the 3-D graphs were obtained using 3000 sub-data are presented in Fig. 4. For a better understanding, the 3D tradeoff Pareto fronts were evaluated from single objectives results. The optimum injector length of 614 mm was fixed to analyze the effects of injection angle and CAI on the change in the average surface temperature of the melt and the fine coal mass input to melt surface. As seen from Fig. 4a, where the injection angle and the CAI were - 45° and 80°, respectively, and the average surface temperature of the melt increases up to 1900K. It was seen that where the injection angle was the same (- 45°) and the CAI was 60°, the average surface temperature of melt (1899 K) has a very close value with the case that had - 45° of injection angle and the 60° of CAI, which is about 1900 K. From Fig. 4b, it was seen that the coal mass input to melt reached the maximum value of 0.39 kg/s where the injection angle was - 45° and the CAI was 60°. While the average surface temperature of melt was the same for two design points where both have the same injection angle of - 45° and have CAI

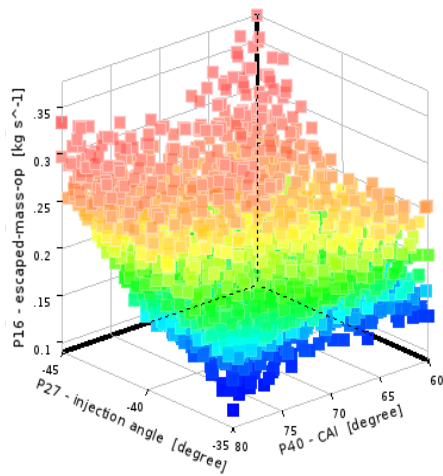
of 80° and 60° however, coal mass input to melt (0,305 kg/s) for CAI of 80° was lower than for CAI of 60° (0.39 kg/s). As a result, for the maximum average surface temperature of the melt and for the maximum fine coal mass input to melt, the optimum injection angle and CAI were determined as -45° and 60°, respectively.

The effects of the injector length and the injection angle on the average surface temperature of the melt and the fine coal mass input to melt are given in Fig. 5 for the fixed value of optimum CAI of 60°. Accordingly, it was seen that the average surface temperature of melt reached the highest value with the injection angle of -40° and the injector length of 510 mm. It was also observed that the fine coal mass input to melt was reached the highest value with the injection angle of -45° and the injector length of 614 mm. These cases, which had the maximum average surface temperature of melt but the very low fine coal mass input to melt, were excluded from the optimum design values. In addition, since the average surface temperature of melt was high in the regions where the fine coal mass input to melt was also high, the optimum values were determined as the injection angle and injector length as -45° and 614 mm, respectively.

The temperature contours at the melt surface were obtained by CFD simulations for the standard (a-



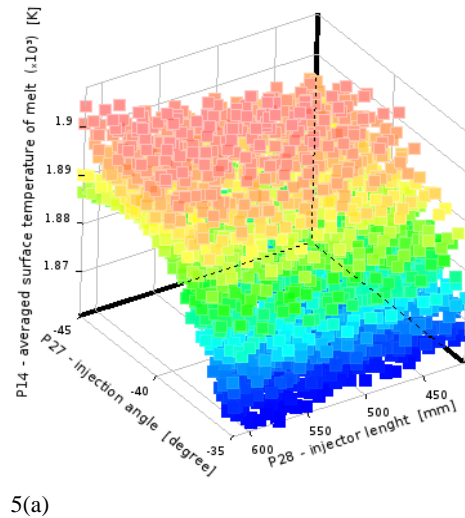
4(a)



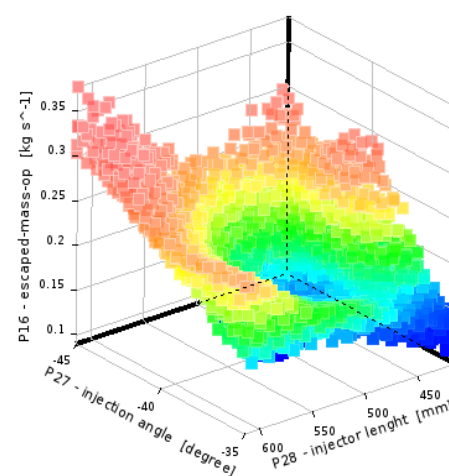
4(b)

Fig. 4. Pareto fronts for the average surface temperature objective (a) and fine coal mass input to melt (b) with injection angle and CIA for the optimum injector length of 614 mm.

injection angle of -45° , the injector length of 514 mm, CAI of 70° and the optimized (b- injection angle of -45° , the injector length of 614 mm, CAI of 60°) injector positions are given in Fig. 6. It is clearly seen that the surface temperature distributions obtained for the optimized injectors have wider and hotter regions than in the standard injectors positioning. The maximum temperature zone which is about 2200 K expanded more below injector 1 and 3 regions. Furthermore, hot region expanded in the middle of the melt surface. It is understanding that the temperature of the area below the injector 2 has slightly decreased. These results show that separate optimization for each injector could give better results. It is also understood that the high-temperature zones are caused by the combustion reactions of fine coal and O_2 supplied from the injectors. As mentioned above, it was considered that the cooling effect in the melt resulting from cold fine coal and O_2 entering into the melt surface can be eliminated by getting hotter and larger areas of the high-temperature zones at the surface of the melt.



5(a)



5(b)

Fig. 5. Pareto fronts for the average surface temperature objective (a) and fine coal mass input to melt (b) with injection angle and injector length for the optimum CAI of 60° .

Probability density functions (PDFs) of the melt surface temperature were created to compare standard and optimized injector sets are presented in Fig. 7. Homogeneity of the temperature distribution is an important factor for the metallurgical characteristics of the melt. It is evident from the PDFs that the slug surface temperature distribution of optimized injector results begins at 1756 K which is 20 K higher than the results of the standard injector indicating a larger homogeneity. Furthermore, the PDF of the optimized injector has a top-hat shape and has 20 K higher temperature at the cold regions and approximately 70 K higher temperature at the hot regions than the standard injector position.

4. CONCLUSION

In this study injector position in terms of injection angle, CAI, and injector length optimization study was conducted for a typical EAF by using CFD simulation technique. Results were compared in terms of injector jet contours and numerical results to find optimum polyhedral mesh size for the CFD

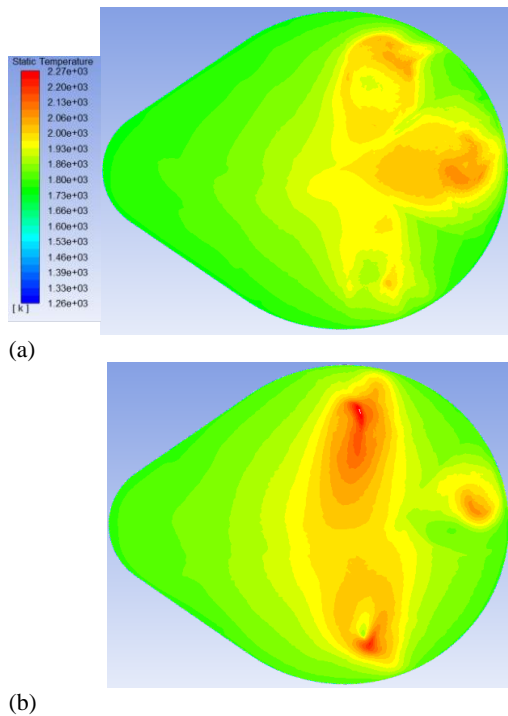


Fig. 6. Melt surface temperature contours obtained from the CFD simulations for standard (a) and optimized (b) injectors.

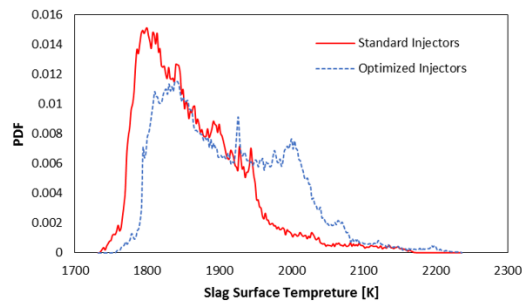


Fig. 7. Melt surface temperature PDF distribution for standard and optimized injectors.

model. For injector position optimization study, injection angle, CAI, and injector length certain parameters were defined in certain ranges and certain intervals. Thus, from the current optimization study;

- 1) Three best solution points were obtained by multi-objective optimization which are maximum average surface temperature and the maximum fine coal input to the melt. As a result, the best solution point for injector length of 614 mm, CAI of 60°, and injection angle of -45°.
- 2) Standard and best injector position sets of surface temperature contours were compared. The result of contours shows that high temperature areas was increased at the optimized injector position.
- 3) The melt surface temperature of PDFs was derived for both standard and optimized injector position. The result of PDFs supports

that the melt surface temperature has more homogeny distribution at the optimized set.

In this study, optimization work applied for EAF was used for increase thermal efficiency and decrease the total process time. Similar simulations can apply to optimize an EAF at the design level. It was determined that the optimization using CFD model is fast, reliable, low cost and can give detailed results. This method is a more economical alternative to costly experimental studies and can provide realistic and detailed results.

Melt volume of the EAF didn't include to the computational domain because of the simulation cost and limitations. Therefore, mixing effect of the injectors to the melt and detail reactions in the melt volume couldn't obtained. Furthermore, including coolant pipes and fluid to the model can increase simulation accuracy. Including these additions can provide more realistic simulations in the future work.

ACKNOWLEDGMENTS

This work was supported by grants from the Scientific and Technological Research Council of Turkey (TÜBİTAK) (Project No: 216M295)

REFERENCES

- Alam, M., J. Naser, G. Brooks and A. Fontana (2010). Computational Fluid Dynamics Modeling of Supersonic Coherent Jets for Electric Arc Furnace Steelmaking Process. *Metallurgical and Materials Transactions B*, 41(6), 1354–1367.
- Alexis, J., M. Ramírez, G. Trapaga and P. Jonson, (2000). Modeling of a DC Electric Arc Furnace-Heat Transfer from the Arc., *ISIJ International* 40(11), 1089–1097.
- ANSYS Fluent 12.0 Theory Guide* (2009) ANSYS, Inc.
- ANSYS Fluent User Manual* (2013) ANSYS Inc.
- Askarova, A., A. Bekmukhamet, S. Bolegenova, S. Ospanova, B. Symbat, V. Maximov, M. Beketayeva and A. Ergalieva (2016). 3-D Modeling of Heat and Mass Transfer during Combustion of Solid Fuel in Bkz-420-140-7C Combustion Chamber of Kazakhstan. *Journal of Applied Fluid Mechanics* 9(2), 699-709.
- Carmona, M. and C. Cortés (2014). Numerical Simulation of a Secondary Aluminum Melting Furnace Heated by a Plasma Torch. *Journal of Materials Processing Technology* 214(2), 334–346.
- Çamdali, Ü. and M. Tunç (2001). Exergy analysis and efficiency in an industrial AC electric ARC furnace. *Applied Thermal Engineering* 23 (17), 2255-2267.
- Falahatkar, S. and H. Ahmadikia (2014). Thermal Analysis of Superheater Platen Tubes in Boilers. *Journal of Applied Fluid Mechanics*

- 7(2), 197-208.
- Fruehan, R. J. (1998). *The Making, Shaping and Treating of Steel: Steelmaking and Refining* Pittsburgh, USA.
- Guo, D. and G. Irons (2003). Modeling of Radiation Intensity an EAF, in: *Third international conference on CFD in the Minerals and Process Industries*. Melbourne, Australia.
- Hites, B. E. (2020). The growth of EAF steelmaking. Recycling Today. <https://www.recyclingtoday.com/article/the-growth-of-eaf-steelmaking/> Accessed:16-12-2020
- Kim, S. E., D. Choudhury and Patel, B. (1997). Computations of Complex Turbulent Flows Using the Commercial Code ANSYS FLUENT, In *Proceedings of the ICASE/LaRC/AFOSR Symposium on Modeling Complex Turbulent Flows*, Hampton, Virginia.
- Kipepe, T. M. and Pan X. (2014). Importance and Effect of Foaming Slag on Energy Efficiency. *71st World Foundry Congress*. Bilbao, Spain.
- Launder, B. E. and D. B. Spalding (1972). *Lectures in Mathematical Models of Turbulence*. Academic Press, London, England.
- Lee, H., S. Choi and B. Kim (2010). Understanding Coal Gasification and Combustion Modeling in General Purpose CFD Code. *Journal of the Korean Society of Combustion* 15(3), 15-24.
- Li, Y. and R. Fruehan (2003). Computational Fluid Dynamics Simulation of Post Combustion in the Electric Arc Furnace. *Metallurgical and Materials Transactions B* 34(3), 333–343.
- Odenthal, H. J., A. Kemminger, F. Krause and N. Vogl (2017). A Holistic CFD Approach for Standard and Shaft-Type Electric Arc Furnaces. *Iron and Steel Technology Conference*, Nashville, USA.
- Pretorius, E. B. and R. C. Carlisle (1998). *Foamy Slag Fundamentals and Their Practical Application to Electric Furnace Steelmaking*. 56th Electric Furnace Conferenca. New Orleans, USA.
- Rahman, M. M. (2010). *Fundamental Investigation of Slag/Carbon Interactions in Electric Arc Furnaces Steelmaking Process*. New South Wales: University of New South Wales, Faculty of Science School of Materials Science and Engineering.
- Sanche, J. L. G., A. N. Conejo and M. A. Ramirez-Argaez (2012). Effect of Foamy Slag Height on Hot Spots Formation inside the Electric Arc Furnace Based on a Radiation Model. *ISIJ International* 2(5), 804–813.
- Scheepers, E., Y. Yang, Allert A. T., R Boom and M. A. Reuter (2010). Process Modeling and Optimization of a Submerged Arc Furnace for Phosphorus Production. *Metallurgical and Materials Transactions B* 41(5), 990–1005.
- Shih, T. H., W. W. Liou, A. Shabbir, Z. Yang, J. Zhu (1995). New k- ϵ Eddy-Viscosity Model for High Reynolds Number Turbulent Flows, Model Development and Validation. *Computers Fluids* 24(3). 227-238.
- Wang, Z, Y. Fu, N. Wang and L. Feng (2014). 3D Numerical Simulation of Electrical Arc Furnaces for the MgO Production. *Journal of Materials Processing Technology* 214(11), 2284–2291.
- Wei, G., R. Zhu, X. Wu, L. Yang, K. Dong, T. Cheng, and T. Tang (2018). Study on the Fluid Flow Characteristics of Coherent Jets with CO² and O² Mixed Injection in Electric Arc Furnace Steelmaking Processes. *Metallurgical and Materials Transactions B: Process Metallurgy and Materials Processing Science* 49(3), 1405–1420.
- Worldsteel Association. <https://www.worldsteel.org/media-centre/press-releases/2020/Global-crude-steel-output-increases-by-3.4--in-2019.html>. Accessed:16-12-2020
- Yangaz, M. U., G. A. Çiftçioğlu and M. A. N. Kadirgan (2019). Comparison of Conventional and Modified Burners in Performance with Different Fuels using a Linear and a Non-linear Eddy-viscosity Turbulence Model. *Journal of Applied Fluid Mechanics* 12(6), 2069-2081.
- Yigit, C., G. Coskun, E. Buyukkaya, U. Durmaz and H. R. Güven (2015). CFD Modeling of Carbon Combustion and Electrode Radiation in an Electric Arc Furnace. *Applied Thermal Engineering* 90, 831-837.
- Zhang, J., W., Prationo, L. Zhang and Z. Zhang (2013). Computational Fluid Dynamics Modeling on the Air-Firing and Oxy-Fuel Combustion of Dried Victorian Brown Coal. *Energy & Fuels* 27(8), 4258-4269.